Acta Geotechnica
https://doi.org/10.1007/s11440-020-00988-8

RESEARCH PAPER

A rate-dependent model for sand to predict constitutive response and instability onset

Mousumi Mukherjee[1] · Anurag Gupta[2] · Amit Prashant[3]

Received: 24 February 2020 / Accepted: 17 May 2020

Abstract
A constitutive model has been proposed for predicting rate-dependent stress–strain response of sand and further implemented in finite element code to explore the influence of strain rate on the localization behavior of sand. The proposed model simulates various constitutive features of sand subjected to higher strain rates, e.g., enhanced shear strength, early peak followed by a softening response, reduced compression for loose sand, etc., which have been reported in the literature. Numerical simulations predict a delayed onset of strain localization and increase in the band angle with increasing strain rate. Strains are noticed to localize in the hardening regime for loose sand, whereas for denser state localization emerges in the post-peak regime.

Keywords High strain rate · Localization · Rate-dependent response · Sand · Viscoplasticity

1 Introduction

The rate-dependent response of geomaterials becomes imperative while modeling the soil behavior under transient and dynamic events such as blast, earthquakes, aircraft wheel loadings on runways and fast installation processes involved in pile foundation or tunneling. The existing literature reveals that at quasi-static regime (10^{-8}–10^{-4}/s), the strength and deformation response of sand is sensitive to the changes in strain rate rather than to the magnitude of the strain rate itself [5, 16, 17, 28, 50]. Stress–strain response of sand has been noticed to differ significantly in transient tests with strain rates varying from 10^{-5} to 1/s or even higher [1, 13, 25, 30–32, 46, 53–55, 58, 59].

Although many of the earlier studies suffer from insufficient instrumentation and measurement issues at higher rates under transient loading, a general trend of increased strength (10–20%) is generally reported at high strain rate [38, 47, 53]. Such strength increase in dry sand was associated with an increase in the peak friction angle, initial shear modulus and an early peak followed by enhanced post-peak softening [1, 13, 25, 32, 54, 55]. Furthermore, a reduced compressive response has also been reported at higher strain rate which under saturated condition resulted in a noticeable increase in the undrained shear strength (30–40%) of loose sand [54, 58]. Rate effects in loose sand were evident at lower confinements, whereas they were more significant for dense sands at higher confinement [32, 46, 59]. At lower confinements, reduced compressive response and inertial and viscous effects are the primary reasons behind rate effects under transient loading [53]. However, a marked increase in transient strength of dense sand under higher confinement is associated with the influence of strain rate on particle crushing [26, 30, 31, 58, 59]. The shape and gradation of sand can also influence the rate-sensitive response [29]. The failure and instability behavior of sands at higher rates is relatively less explored; however, in case of coral sand Yamamuro

✉ Amit Prashant
ap@iitgn.ac.in

Mousumi Mukherjee
mousumi@iitmandi.ac.in

Anurag Gupta
ag@iitk.ac.in

[1] School of Engineering, Indian Institute of Technology Mandi, Mandi, India

[2] Mechanical Engineering, Indian Institute of Technology Kanpur, Kanpur, India

[3] Civil Engineering, Indian Institute of Technology Gandhinagar, Gandhinagar, India

Published online: 06 June 2020

et al. [59] noticed an early onset of localization and decreasing trend in shear band angle with an increase in the strain rate. On the contrary, Watanabe and Kusakabe [53] observed the failure mode in Toyoura sand at low strain rate to be bulging with distinct shear band formation due to strain localization, which changed into a diffused bulging-type failure when subjected to higher strain rate. Based on the biaxial experiments on saturated St. Peter Sandstone sand, Han and Vardoulakis [21] argued that the presence of small amount of strain rate sensitivity can provide stability against liquefaction phenomenon near the peak deviatoric stress. Theoretical studies of Garagash [20] also indicated that degree of rate sensitivity, along with the ratio of the material pore diffusion length scale to the specimen size, decides whether the final failure mode will be a diffused or localized one.

The rate-dependent response of sand is generally modeled within elasto-viscoplastic framework, which can be broadly classified into two categories. The first category is of the overstress models based on the viscoplastic constitutive equations proposed by Perzyna [40, 41]. Rate-dependent sand models formulated under this category are basically an extension of commonly used critical state models with the modified flow rule to take into account the evolution of viscoplastic strain rate [4, 11, 15, 23, 27, 51]. The second category of viscoplastic models is developed for general prediction of any time-dependent phenomenon, e.g., creep or step-changed loading [16, 17, 29, 39, 50]. Such models are mostly empirical or semiempirical in nature where nonlinear functions are used to represent the delayed stress–strain response with time. The experimental observations of sand at high strain rate exhibiting strength increase along with early peak, followed by enhanced rate-induced softening and reduced compressive response, are not aptly captured by these models. Furthermore, the influence of strain rate on failure and instability behavior of sand is yet to be explored.

A rate-dependent constitutive model has been proposed here for predicting stress–strain response of sand at high strain rate. In order to include rate dependency, Perzyna-type framework has been used to modify the flow rule of the underlying 3D non-associative rate-independent material model of Wood et al. [57] and Wood [56]. A small deformation formulation has been employed for predicting the rate-dependent response. The influence of model parameters on prediction of such rate-dependent response has been assessed through simulation of biaxial test with varying strain rates. In this regard, the uniform stress–strain prediction of the model has been examined at two different initial densities and confining pressure. The proposed model further has been employed to predict the constitutive response of two different soils at different strain rates under triaxial loading condition, and the same has been compared against the experimental data available in the literature. In addition, the model has been implemented in ABAQUS, commercially available finite element software, by writing a user-defined material model subroutine (UMAT). Simulations are carried out to predict localized instability response of sand at varying strain rates.

2 Proposed rate-dependent model

2.1 Mathematical formulation

Wood et al. [57] proposed a 3D non-associative constitutive model based on critical state concept which includes both shear and volumetric hardening. Recently, Mukherjee et al. [33, 34] performed a large deformation-based plane-strain bifurcation analysis employing this model in order to explore various drained and undrained instabilities in sand when subjected to biaxial loading condition. The model fairly captured the stress–strain and volumetric response of sand along with different instability modes, i.e., diffused, localized and/or solid–fluid instabilities at various densities and confinement. The rate-dependent constitutive relations are formed here within small deformation framework, and a Perzyna-type overstress formulation has been adopted here for extending the rate-independent constitutive model of Wood et al. [57] and Wood [56] to a rate-dependent form. The dynamic (f_d) and static (f_s) yield surfaces take the following form:

$$f_d = \sqrt{3J_2} - \eta_{yd}\frac{I_1'}{3} = 0\,, \tag{1}$$

$$f_s = \sqrt{3J_2} - \eta_{ys}\frac{I_1'}{3} = 0\,, \tag{2}$$

where I_1' is the first invariant of effective stress tensor (σ'), J_2 is the second invariant of deviatoric stress tensor and η_{yd} and η_{ys} represent the dynamic and static shear stress ratios, respectively (Fig. 1). The dynamic stress ratio is related to the current stress state and the viscoplastic strain starts to evolve when $\eta_{yd} \geq \eta_{ys}$. The plastic potential is given by

$$g_d = \sqrt{3J_2} - M_C\frac{I_1'}{3}\ln\frac{3P_r'}{I_1'} = 0\,, \tag{3}$$

where M_C is the slope of the critical state line and P_r' is the intercept of plastic potential on the $I_1'/3$ axis. In case of overstress model, the evolution of viscoplastic strain (ε^{vp}) is generally captured by introducing an exponential or power-law-type relation [11, 24, 37]. Furthermore, the high-strain-rate experiments in sand revealed that the peak stress ratio varies nearly linearly over the logarithmic scale of strain rate [32, 46, 59]. Following this observation, we

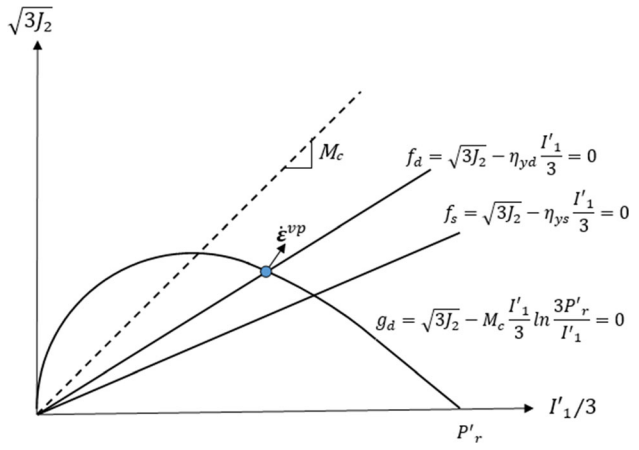

Fig. 1 Static and dynamic yield surface, plastic potential in the stress space

have employed a power-law-type relation for modifying the flow rule which is given as

$$\dot{\varepsilon}_{ij}^{vp} = \dot{\varepsilon}_{\text{ref}}\left(\frac{\eta_{\text{yd}}}{\eta_{\text{ys}}}\right)^{n}\frac{\partial g_{\text{d}}}{\partial \sigma'_{ij}} \ , \ \text{when} \ \frac{\eta_{\text{yd}}}{\eta_{\text{ys}}} \geq 1 \ . \tag{4}$$

Here, $\dot{\varepsilon}_{\text{ref}}$ and n are the reference axial strain rate and power law exponent controlling the rate-dependent behavior. The strength increase at any strain rate is mapped with respect to the chosen reference strain rate parameter. A lower value of reference strain rate and power law exponent reflects higher sensitivity toward strain rate. Similar to rate-dependent model, η_{ys} depends on the accumulated viscoplastic shear strain ε_q^{vp}, and its evolution is governed by the following hyperbolic hardening law:

$$\frac{\eta_{\text{ys}}}{\eta_{\text{ps}}} = \frac{\varepsilon_q^{vp}}{a + \varepsilon_q^{vp}} \ , \tag{5}$$

where a is the material parameter and η_{ps} is the static peak shear stress ratio. Here, η_{ps} is a function of another state variable ψ, which represents relative density of sand in some sense and includes information of specific volume v_e and mean stress

$$\eta_{\text{ps}} = M_{\text{C}} - \kappa\psi = M_{\text{C}} - \kappa\left[v_e - \Gamma + \Lambda_{\text{C}}\ln\left(\frac{I'_1}{3}\right)\right] \ , \tag{6}$$

where κ is the material constant, Λ_{C} is the slope of the critical state line in compression plane and Γ is the intercept of the critical state line on the specific volume axis at mean pressure level of 1 kPa. It has been assumed for simplicity that the elastic volumetric strain roughly balances the effect of the change in mean effective stress [56]. Hence, only the dependence of η_{ps} on viscoplastic volumetric strain ε_p^{vp} has been taken into account. The subsequent sections present the rate-dependent stress–strain response predicted by the model at varying strain rates for different confining pressures and density states.

2.2 Model response under biaxial condition

A code has been written in MATLAB to predict the rate-dependent uniform stress–strain behavior of sand in drained biaxial test. A one-step forward Euler stress-update algorithm [52] has been used to numerically integrate the rate-dependent constitutive relations given in the previous section. Details of the algorithm and related derivations are discussed in "Appendix". Numerical integration requires a threshold time step for convergence, and its magnitude is found to be smaller for higher rates. A typical time discretization number of $\dot{\varepsilon}_{a,\max}/10\dot{\varepsilon}_{\text{ref}}$ has been employed for all the simulations, where $\dot{\varepsilon}_{a,\max} = 0.1$/s. The trends of rate-dependent stress–strain and volumetric response are predicted at two different densities ($e_0 = 0.9$ and $e_0 = 0.65$) and confinement (100 and 300 kPa) based on assumed values of rate-dependent parameters, i.e., reference strain rate ($\dot{\varepsilon}_{\text{ref}}$) and power law exponent (n). The rate-independent model parameters are given in Table 1 which conform to the properties of Hostun RF sand [19, 56], and the assumed values of rate-dependent parameters are $\dot{\varepsilon}_{\text{ref}} = 1 \times 10^{-6}$/s and $n = 60$.

Figure 2 shows the evolution of stress–strain behavior, volumetric response and the state variable η_{ps}, i.e., static peak shear stress ratio with continued shearing for loose sand ($e_0 = 0.9$) with 300 kPa confining pressure. Similar to the experimental observations reported by Omidvar et al. [38] and Watanabe and Kusakabe [53], increasing shear

Table 1 Material constants considered for the biaxial test simulation [19, 56]

Parameter	Description	Value
μ	Shear modulus	$G_0/3$**
ν	Poisson's ratio	0.1
M_{C}	Slope of critical state line in $\sqrt{3J_2} - I'_1/3$ plane	1.2
Λ_{C}	Slope of critical state line in specific volume (v_e) $-$ ln($I'_1/3$) plane	0.03
Γ	Intercept for critical state line in $v_e - \ln(I'_1/3)$ plane at 1 kPa effective mean pressure	1.969
a	Parameter controlling hyperbolic stiffness relationship	0.0016
κ	Relation between changes in state parameter (ψ) and current peak stress ratio (η_{ps})	2

**G_0 is the small strain shear modulus which is function of specific volume v_e and mean effective stress $I'_1/3$ expressed in kPa [56]

$$G_0 = 3230\frac{(3.97 - v_e)^2}{v_e}\sqrt{I'_1/3} \tag{7}$$

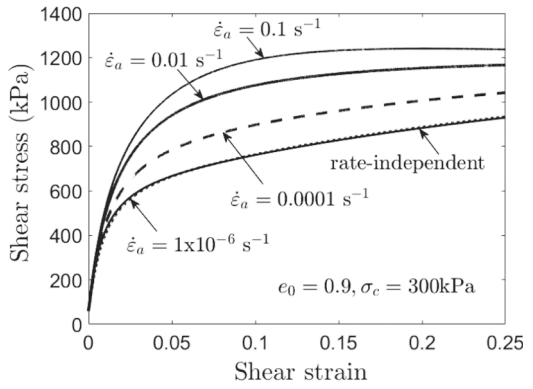

(a)

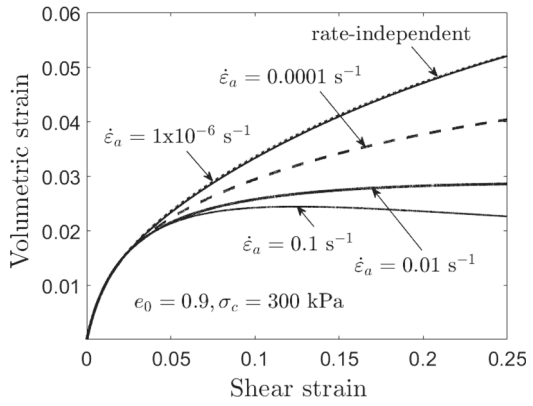

(b)

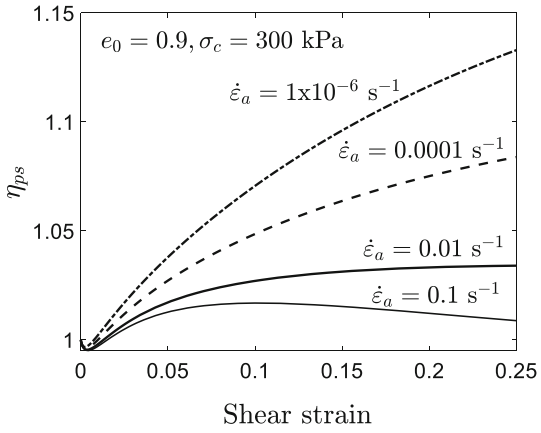

(c)

Fig. 2 Evolution of **a** stress–strain, **b** volumetric response and **c** state variable η_{ps} with varying strain rates at $e_0 = 0.9$ and confining pressure 300 kPa

stress and enhanced dilation can be noticed at any level of shear strain with an increase in strain rate from 1×10^{-6} to 0.1/s. Rate effects on stress–strain response become more evident at lower range of strain in contrast to volumetric behavior, where such effects manifest at larger strain. The pronounced strain hardening response at lower rates gradually diminishes with increasing rate of strain. The state variable η_{ps} controls the shear-based hardening behavior of the material. At higher rates, the enhanced dilation leads to a reduction in η_{ps}, which further results in such reduced hardening response. In case of simulations at reference strain rate 1×10^{-6}/s, the stress–strain response predicted from rate-dependent analysis becomes comparable with the same from rate-independent one (Fig. 2).

Figure 3 depicts the influence of parameter n on stress–strain–volume prediction of loose sand at a lower confinement. As mentioned earlier, a lower value of n results in stronger rate-dependent response. Hence, the simulations with $n = 60$ predict an enhanced strain rate effect in terms of strength increase and less compressive response than those with $n = 200$. The model captures early peaks followed by strain softening response in loose sands at lower confinement for the case with $n = 60$, i.e., simulations with higher rate dependency. This type of behavior was also noticed experimentally by Lee et al. [32] and Yamamuro et al. [59]. At higher n values, the rate-induced strength increase remains nearly uniform with continued shearing; however, similar to lower n values the rate effects on volumetric response become more evident with accumulated strain during shearing. This is also consistent with the experimental observations of Yamamuro et al. [59] and Watanabe and Kusakabe [53]. The rate parameters n and $\dot{\varepsilon}_{ref}$ may vary over different strain rate regimes, and such variations can be captured through experiments. It is important to note that the proposed model can be used to predict rate-dependent response over both low and high range of strain rate, provided the rate parameters are selected carefully over the considered strain rate regime.

The predicted behavior of dense sand with varying strain rates is shown in Fig. 4. Similar to loose case, at any level of strain higher strain rate results in an increase in shear stress. However, delayed stress peaks are noticed in such cases with stronger post-peak softening. Unlike loose sand, increased strain rate leads to the prediction of reduced dilative response in dense sand. This behavior remains unchanged even at higher confinements. Though experimental observation of rate effects in dense sand is limited, the existing literature suggests that the rate-induced strength increase in dense sand is less pronounced than in loose state [32]. Such change in strength can be incorporated by calibrating the rate parameter, n over different density ranges. The power law exponent becomes an important parameter since it controls the applicability of the model for different density states and various ranges of strain rate, medium to high strain rate.

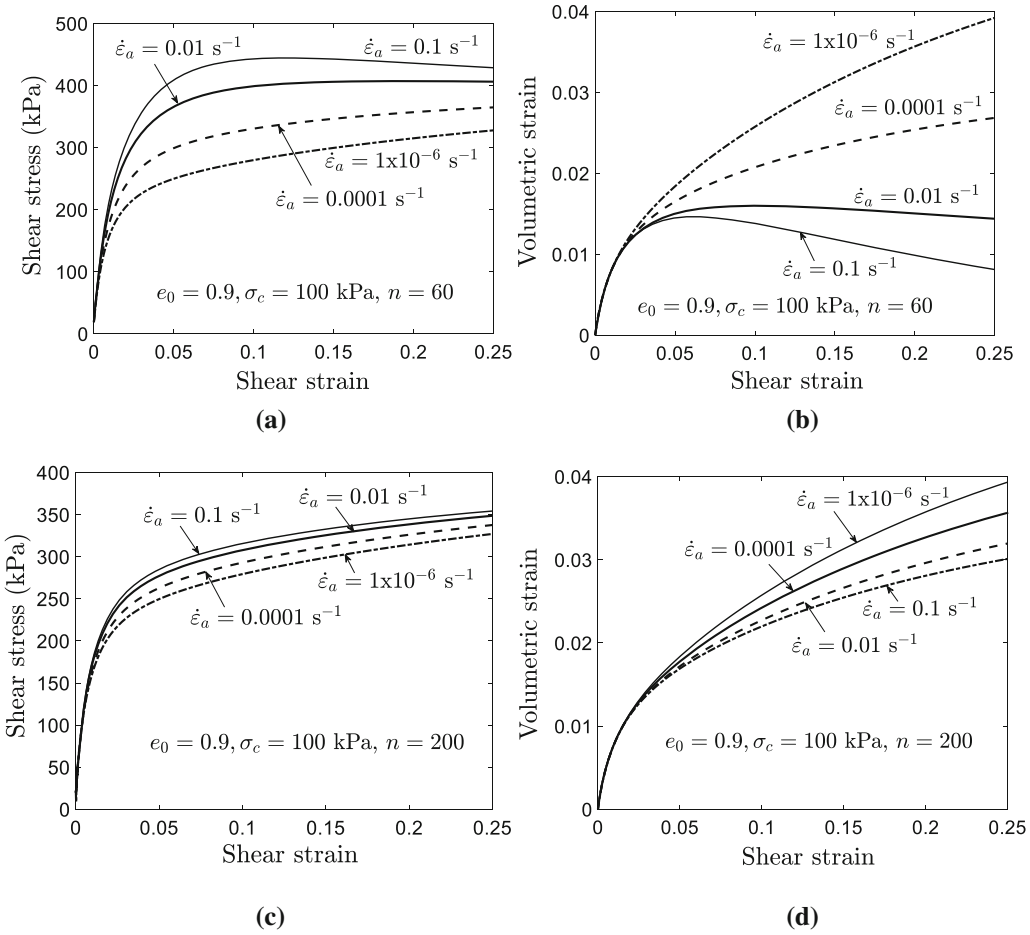

Fig. 3 Evolution of **a**, **c** stress–strain, **b**, **d** volumetric response with varying strain rates at $e_0 = 0.9$ and confining pressure 100 kPa for two n values

3 Validation of proposed model against experimental observation

There are only a few studies available on the rate-dependent behavior of sand and moreover, and their experimental data are not sufficient for a comprehensive calibration of all the model parameters. The model predictions are compared in this section against the triaxial experimental data on crushed coral sand and silica sand as reported in Yamamuro et al. [59] and Suescun-Florez and Iskander [46], respectively.

For the dry crushed coral sand, the stress–strain and volumetric response in triaxial test was reported for two different density states, i.e., RD = 58% ($e_0 = 0.94$) and 36% ($e_0 = 1.03$), each subjected to initial confining pressures of 98 and 350 kPa. The experiments were performed at different strain rates ranging from 0.0022 to 1764%/s. The variation in the peak stress ratio over these strain rate ranges is plotted in Fig. 5a. It can be noticed that the peak stress ratio nearly remains unaffected by the strain rate below 0.23%/s, which has been considered as the reference strain rate ($\dot{\varepsilon}_{\text{ref}}$) for simulation of stress–strain and volumetric response of coral sand. Beyond the reference strain rate, the stress ratio increases linearly over logarithmic increase in the strain rate magnitude which further justifies the implementation of the power-law-type flow rule in rate-dependent enhancement of the critical state model. Figure 5b presents the peak shear stress values from different strain rates normalized by the peak value at the lowest strain rate. Similar to the stress ratio, a sharp increase in the peak shear stress value is evident beyond the reference strain rate and such increase is more significant at higher confinement. The average slope of the semi-logarithmic curves of Fig. 5b beyond the reference strain rate $\dot{\varepsilon}_{\text{ref}} = 0.23\%/\text{s}$ has been calculated, and it tentatively represents the magnitude of the power law exponent, $n = 42$. The rate-independent material parameters for coral sand have been estimated iteratively to match the stress–strain response at $\dot{\varepsilon}_{\text{ref}} = 0.23\%/\text{s}$ for the case with RD = 58% using the triaxial data of two different magnitudes of confining pressure [59]. The calibrated constitutive model parameters for the coral sand are listed in Table 2. Due to

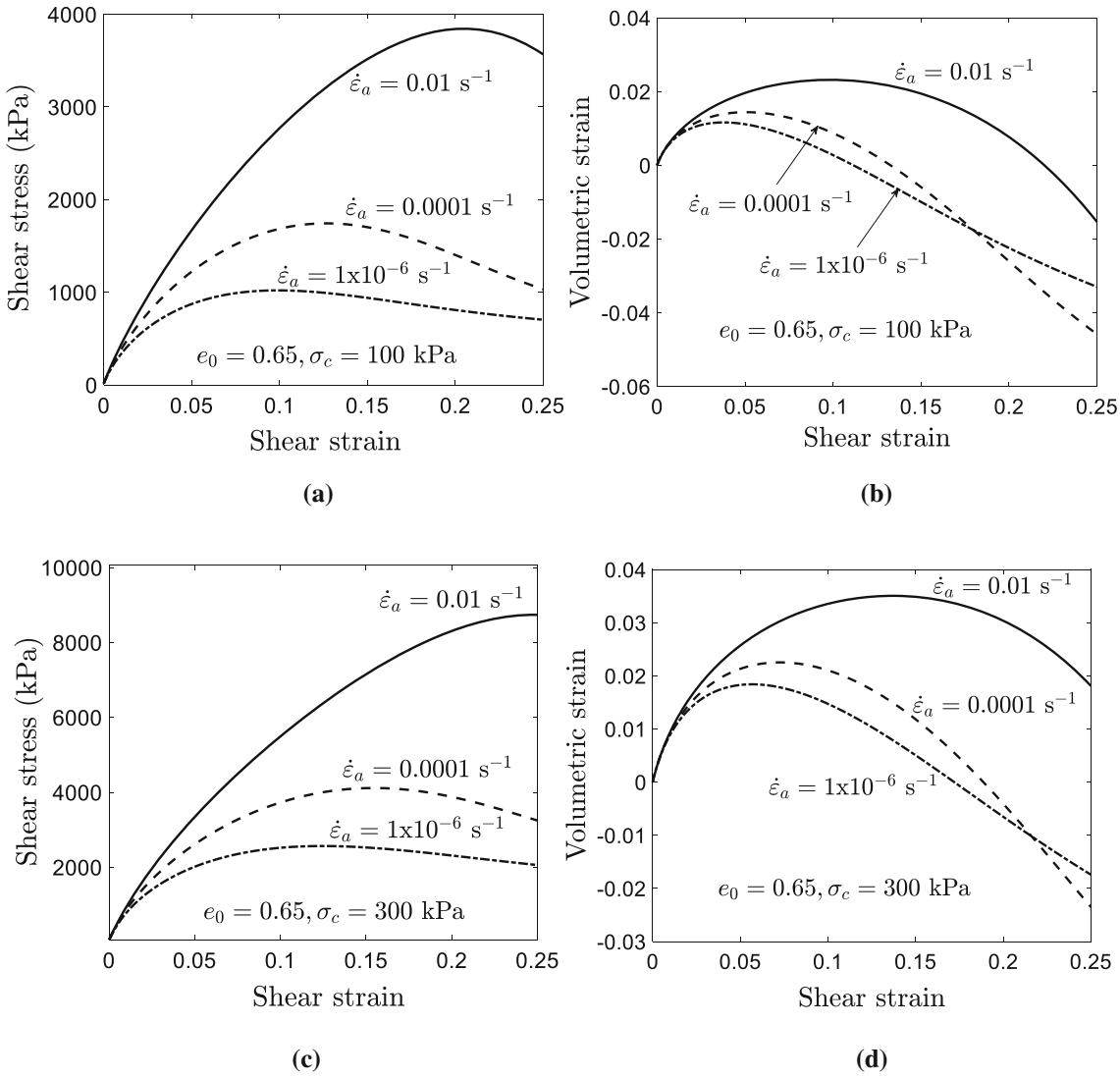

Fig. 4 Evolution of **a**, **c** stress–strain, **b**, **d** volumetric response with varying strain rates for $e_0 = 0.65$ at confining pressures 100 and 300 kPa, respectively

limited data, simultaneous calibration against both stress–strain and volumetric response could not be carried out rigorously. The focus was mainly to mimic the stress–strain response by trading off the volume change behavior prediction. As a result, more deviation from the experimental data was noticed in case of the volumetric behavior even for the rate-independent response predicted at the reference strain rate. The comparison of simulated stress–strain and volumetric response for varying strain rates at different relative densities and confining pressures is depicted in Fig. 6. It can be noticed that the model can aptly capture the rate-dependent stress strain response of the sand for both the density states, which includes strength increase at higher strain rate, early peak followed by a softening response. The predicted magnitude of peak stresses and their strain levels are also comparable with the experimental data. The model can fairly mimic the general trend in volumetric behavior with increasing strain rate, i.e., reduced compression and dilation at lower and higher density, respectively. In this regard, it is important to note that the proposed rate-dependent model has been framed following the Perzyna-type overstress formulation, which has been widely applied for predicting the viscoplastic behavior of metals. In this type of formulation, the strength enhancement over the varying ranges of strain rate gets captured through the power law exponent which in turn permits only limited control for replicating the rate-induced volume change characteristics to an extent.

A similar comparison has also been carried out for silica sand based on the triaxial test data reported by Suescun-Florez and Iskander [46] at four different strain rates, 0.01%/s, 0.1%/s, 1%/s and 10%/s. Two density states,

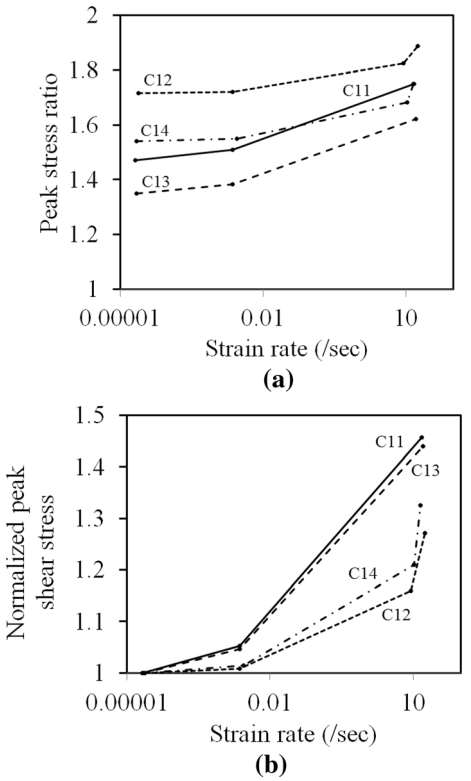

Fig. 5 Variation in **a** peak stress ratio and **b** normalized peak shear stress of dry crushed coral sand during triaxial test at varying strain rates [59], where different indices stand for combination of density and confining state: C11 (RD = 58%, $\sigma_c = 350$ kPa), C12 (RD = 58%, $\sigma_c = 98$ kPa), C13 (RD = 36%, $\sigma_c = 350$ kPa), C14 (RD = 36%, $\sigma_c = 98$ kPa)

RD = 85% ($e_0 = 0.53$) and 55% ($e_0 = 0.63$), with 400 kPa initial confining pressure have been considered for the validation. The peak shear stress response, normalized by the peak shear stress at 0.01%/s, is plotted against the strain rate range in Fig. 7a for these two density states. It can be noticed that the rate-induced strength increase is more prevalent for the dense sand compared to the loose one. The average slope of the two curves given in Fig. 7a has been estimated as $n = 28$, and the lowest strain rate 0.01%/s has been considered as the reference strain rate. Due to lack of information in the literature regarding the volumetric response, rate-independent material parameters have been extracted iteratively to match solely the stress–strain behavior at $\dot{\varepsilon}_{\text{ref}} = 0.01\%/\text{s}$. The calibrated model parameters are given in Table 3, and the predicted stress–strain responses are depicted in Fig. 7b, c. It can be observed that the experimental trends have been replicated well by the proposed model predictions.

4 Instability prediction with varying strain rates

Influence of strain rate on the localized instability mode has been investigated by using the proposed rate-dependent model. First, possible initiation of such instabilities has been examined based on the uniform stress–strain response. Thereafter, the model has been implemented in a finite element framework to explore the emergence of strain localization in the form of shear bands.

4.1 Instability from uniform stress–strain response

In case of Perzyna-type rate-dependent model, the consistency condition cannot be applied directly to the evolution of dynamic yield surface [14, 48]. As a result, an explicit expression for elasto-viscoplastic tangent stiffness modulus cannot be formed in this case. This further restricts application of global bifurcation-based instability approach to a rate-dependent formulation. Following the local bifurcation framework of Bigoni [6], the loss of positiveness of second-order work criteria, i.e., $d\sigma_{ij}d\varepsilon_{ij} \leq 0$, can be employed to identify the initiation of instability in rate-dependent problems [18]. Figure 8 presents the evolution of second-order work in biaxial test at two different densities for the parameter set given in Table 1. In case of loose sands, an increase in the strain rate results in faster loss of positiveness of second-order work, whereas for dense sand it gets delayed with increasing strain rate. However, this criterion is not sufficient for ensuring onset of localized modes, which is generally obtained from loss of positive definiteness of acoustic tensor [36, 45, 49]. As no explicit expression can be formed for tangent stiffness tensor, it is not possible to check analytically the positive definiteness criteria of acoustic tensor in rate-dependent framework. Many of the researchers proposed method for deriving algorithmic tangent stiffness tensor for viscoplastic models [12, 22, 42, 52]. The algorithmic tangent stiffness tensor for the proposed model is given in "Appendix", which is derived based on Wang's [52] formulation. However, the acoustic tensor calculated from algorithmic modulus

Table 2 Calibrated constitutive model parameters used for triaxial simulation of coral sand

Parameter	$\dot{\varepsilon}_{\text{ref}}$(%/s)	n	M_C	Λ_C	Γ	a	κ	ν	μ (GPa)
Value	0.23	42	1.4	0.036	2.25	0.0016	2.8	0.3	$G_0/3$ as estimated from Eq. 7

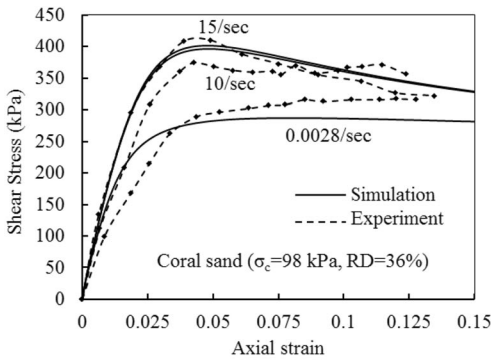
Shear Stress (kPa)
Axial strain
15/sec
10/sec
0.0028/sec
Simulation
Experiment
Coral sand (σc=98 kPa, RD=36%)

(a)

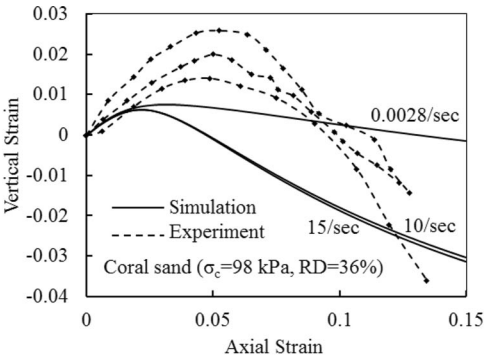
Vertical Strain
Axial Strain
0.0028/sec
Simulation
Experiment
15/sec
10/sec
Coral sand (σc=98 kPa, RD=36%)

(b)

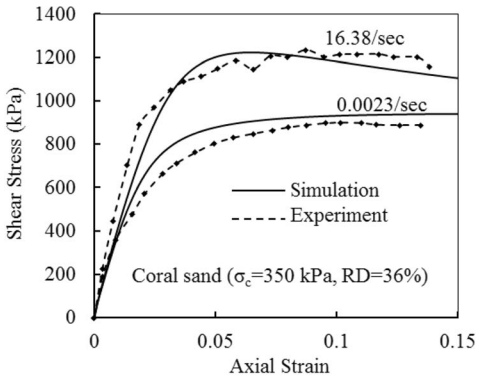
Shear Stress (kPa)
Axial Strain
16.38/sec
0.0023/sec
Simulation
Experiment
Coral sand (σc=350 kPa, RD=36%)

(c)

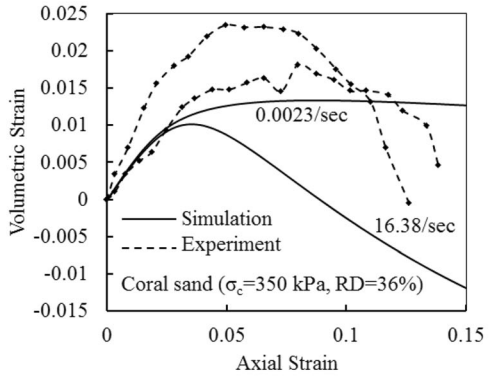
Volumetric Strain
Axial Strain
0.0023/sec
Simulation
Experiment
16.38/sec
Coral sand (σc=350 kPa, RD=36%)

(d)

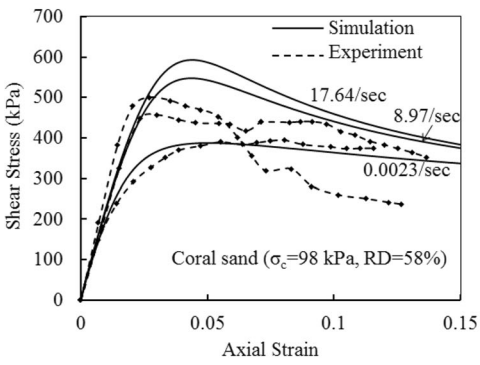
Shear Stress (kPa)
Axial Strain
Simulation
Experiment
17.64/sec
8.97/sec
0.0023/sec
Coral sand (σc=98 kPa, RD=58%)

(e)

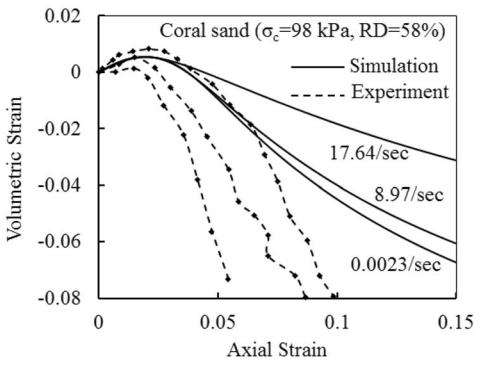
Volumetric Strain
Axial Strain
Coral sand (σc=98 kPa, RD=58%)
Simulation
Experiment
17.64/sec
8.97/sec
0.0023/sec

(f)

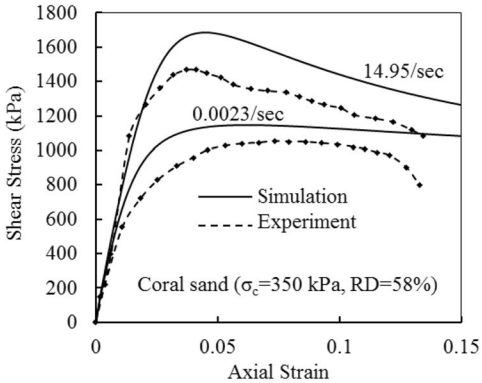
Shear Stress (kPa)
Axial Strain
14.95/sec
0.0023/sec
Simulation
Experiment
Coral sand (σc=350 kPa, RD=58%)

(g)

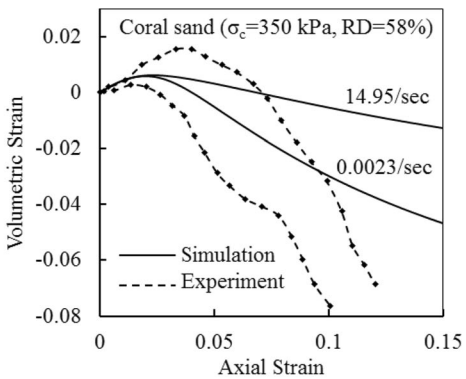
Volumetric Strain
Axial Strain
Coral sand (σc=350 kPa, RD=58%)
14.95/sec
0.0023/sec
Simulation
Experiment

(h)

◀**Fig. 6** Evolution of **a**, **c**, **e**, **g** stress–strain, **b**, **d**, **f**, **h** volumetric response of coral sand under triaxial simulation with varying strain rates for two relative densities (RD = 36% and 58%) and confining pressures (σ_c = 98 and 350 kPa)

remains positive definite for Perzyna type of viscoplastic models, which further ensures effectiveness of such models in regularizing the localization behavior [18, 35, 44]. A numerical approach can be adopted to explore the localized type of instability within a rate-dependent framework.

4.2 Instability from finite element simulation

The proposed model has been implemented in ABAQUS v6.12 by writing a UMAT subroutine. Plane-strain 2D simulations are carried out to replicate the biaxial test condition. The model geometry and boundary conditions are shown in Fig. 9. The bottom-most boundary has been kept fixed in x_2 direction, whereas the displacement in x_1 direction has been restricted only for the left bottom-most corner in order to prevent rigid body rotation. The lateral boundaries are subjected to the prescribed level of confining pressure. Loading has been applied in two stages.

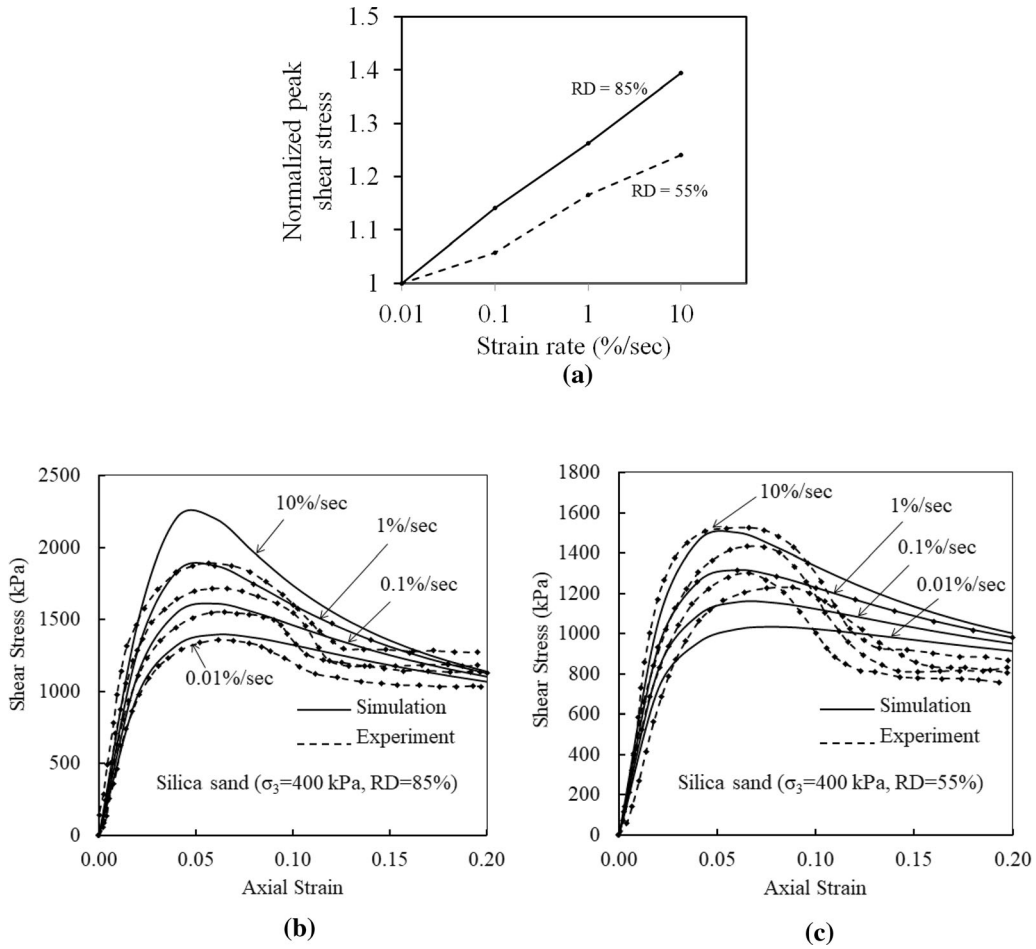

Fig. 7 Variation in **a** normalized peak shear stress of dry silica sand during triaxial test at varying strain rates [46], and its **b**, **c** stress–strain response for two density states at 400 kPa confining pressure

Table 3 Calibrated constitutive model parameters used for triaxial simulation of silica sand

Parameter	$\dot{\varepsilon}_{ref}$(%/s)	n	M_C	Λ_C	Γ	a	κ	ν	μ (GPa)
Value	0.01	28	1.1	0.025	1.94	0.006	3.0	0.3	$G_0/3$ as estimated from Eq. 7

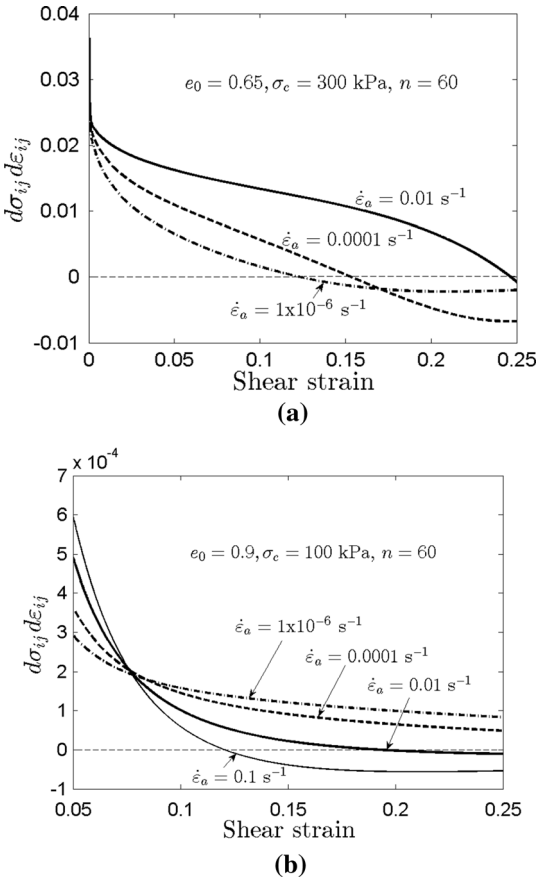

Fig. 8 Loss of positiveness of second-order work for **a** dense and **b** loose sand

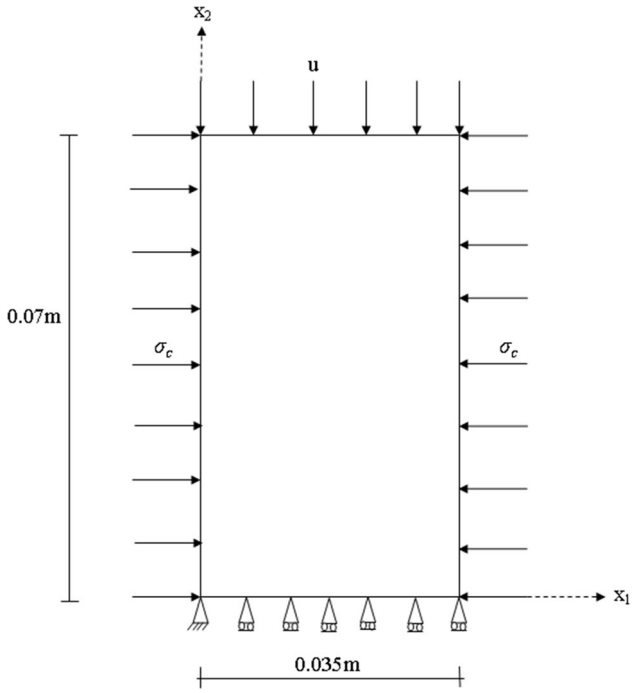

Fig. 9 Finite element model geometry, loading and boundary conditions

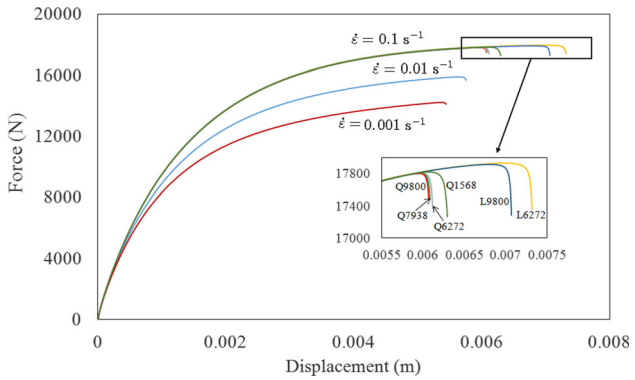

Fig. 10 Force–displacement curves obtained from 2D plane-strain simulations at varying strain rates for biaxial shearing with $e_0 = 0.9$ and 100 kPa initial confining pressure (number of elements are marked with element type, where 'Q' and 'L' stand for quadratic and linear element, respectively)

First, an initial confining pressure has been applied over all the boundaries and the equilibrium condition has been checked under such applied confinement. Next, the shearing phase has been simulated by applying an axial displacement on the topmost boundary such that the strain rate remains constant. A full Newton–Raphson algorithm has been selected for solving the boundary value problem along with an unsymmetrical solver. The finite element simulations have been carried out by employing the set of material parameters listed in Table 1, which are same as used while predicting the uniform stress–strain response under biaxial loading condition in Sect. 2.2. These simulations are first verified against the uniform stress–strain predictions from the MATLAB code. Thereafter, heterogeneity has been induced in the left bottom-most element by locally altering the initial magnitude of the material parameter η_{ys}, i.e., 0.5% less than the global value used for other elements. Such perturbation is necessary to initiate localization in a finite element analysis.

Simulation results in terms of force–displacement curve are presented in Fig. 10 for the biaxial shearing with $e_0 = 0.9$ and 100 kPa initial confining pressure. In these simulations, the assumed values of rate-dependent parameters are $\dot{\varepsilon}_{ref} = 1 \times 10^{-6}$/s and $n = 60$. A convergence study has been performed first to obtain the optimum number of element discretization. For a converged solution, the force–displacement result nearly remains unaffected by the change in mesh discretization. Both linear and quadratic elements are used initially for the simulation at 0.1/s strain rate. Four sets of quadratic elements with the number of elements 1568, 6272, 7938 and 9800 and two sets of linear elements with the number of elements 6272 and 9800 have been considered in the convergence study. Compared to linear elements, the element discretization with quadratic

elements shows faster convergence. The simulation for this case has been considered to be converged for a quadratic meshing with 7938 number of elements, beyond which the force–displacement result nearly remained unaffected by the change in mesh discretization (Fig. 10). The applied strain rate of 0.1/s is the average strain rate which is acting at the top boundary; however, the strain rate within the sample is noticed to differ from this average value. Such

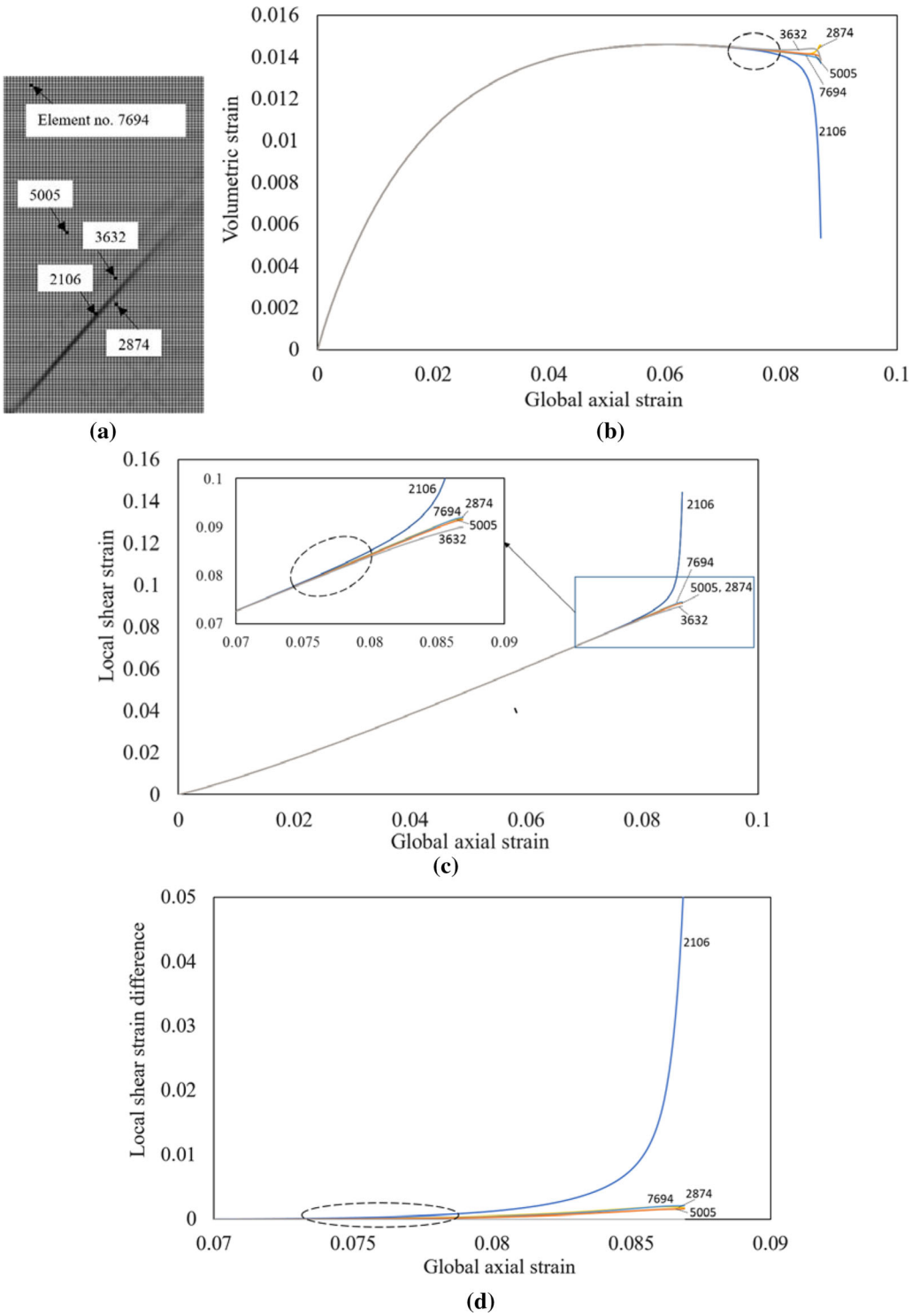

Fig. 11 **a** Elements position and evolution of **b** local volumetric strain, **c** local shear strain and **d** local shear strain difference (measured with respect to element no. 3632) with global axial strain

variation becomes more pronounced with initiation of localization. For example, the local strain rate varies from 0.01 to 8/s when the applied average strain rate is 0.1/s.

The drop in the force–displacement curve indicates the initiation of localized shear band; however, it is difficult to identify the exact initiation point. The sharp drop also marks a deviation from the force–displacement curve of uniform case, which further confirms that the localization may have taken place within the neighborhood of this strain level (8.52% global axial strain). In a series of true triaxial experiments on Kaolin clay, Prashant and Penumadu [43] also noticed a sudden change in the evolution of strain response near the point where specimens were observed to have localized deformations. To examine further, the local shear and volumetric strain has been explored at multiple locations. During the initial phase of the simulation, the non-uniform deformation initiates from the left bottom-most corner, where the material heterogeneity was induced. With the continued deformation, a zone of localized plastic strain emerges which contains the element with initially induced heterogeneity. However, the maximum plastic strain accumulation may not necessarily occur at this location. By examining the evolution of plastic strain across the complete domain, the element 2106 has been identified as the element with the maximum accumulation of plastic strain. Four other elements, located far from the zone of strain localization, have been selected for exploring the local strain variations. The element positions are marked in Fig. 11a, and the local volumetric and shear strain has been plotted against the global axial strain level for gauss points of these five different elements in Fig. 11b, c, respectively. The local shear and volumetric strain of the element no. 2106 starts to differ suddenly from other elements around 7.7% global strain. This particular element lies on the localized zone, and the sudden variation in strain response for this element is a clear indication of localization onset (Fig. 11d). It is to be noted that such approach predicts an early localization onset compared to the global force–displacement approach. Hence, the local variations can be used effectively to identify the bifurcation onset within a numerical framework. Figures 14a and 16a present a comparison of localization onset predicted by these two methods over different ranges of strain rate and n values. It can be observed from Fig. 11b that once the localization commences, the volumetric deformation primarily takes place within the localized zone exhibiting a sharp reduction in compressive response with continued shearing. A gradual reduction in compressive response is also visible in elements far from the localized zone, i.e., shear band (element nos. 7694, 5005, 3632). However, an enhanced compressive response is noticed at elements nearer to the shear band (element no. 2874).

Fig. 12 Shear band developed for two quadratic mesh discretizations with the number of elements **a** 7938 and **b** 9800 which are simulated at 0.1/s strain rate with $e_0 = 0.9$ and $\sigma_c = 100$ kPa (shear strain contour at 8.7% global axial strain)

After the mesh convergence, the thickness of the shear band remains independent of the mesh size (Fig. 12). Similar observation is also noted when the heterogeneity has been induced at a different position, e.g., at mid-point of the leftmost surface (Fig. 13). This is a typical attribute of the rate-dependent models which regularizes the localization problem by inducing a length scale due to the presence of inherent timescale [35]. To understand the instability behavior near a perturbed zone and yet keep the analysis simple, the localization in the present study has been initiated by inducing heterogeneity locally at a particular element. However, a more realistic representation of material non-homogeneity can be obtained through random distribution of a material parameter, e.g., spatially varying density states [2, 3, 7, 8] or spatially varying degrees of saturation [9], over the domain. As mentioned earlier, only localized instability can be explored within the present numerical framework due to the assumption of small deformation.

The converged simulation results for two other strain rates, i.e., 0.01 and 0.001/s, are also presented in Fig. 10. It can be observed that for all of these cases, localization emerges in the hardening regime and gets delayed with an increase in the strain rate. Figure 14a presents the variation of global axial strain at localization against axial strain rates in logarithmic scale considering both global and local response. The global response curves for localization onset have been obtained by following the global force–displacement approach, as explained in Fig. 10. The response of element 2106, which exhibited the maximum accumulation of plastic strain, has been used as a local response to indicate the bifurcation onset. The global axial strain was calculated by dividing the applied vertical displacement on the top boundary with respect to the initial height of the biaxial specimen. Due to the existence of non-uniform deformation field, the global axial strain value is different from the local strains, which further varies at different locations within the model domain. Therefore, while comparing the localization onset predictions from two different approaches (global and local response), the global axial strain value at the onset of localization has been considered here as the basis for comparison. A linear variation has been noticed which remains unchanged even at higher confinements (300 kPa). An increase in the confining pressure, however, further retards the emergence of localization. As shown in Fig. 14b, shear band angle also increases with an increase in applied strain rate. In case of

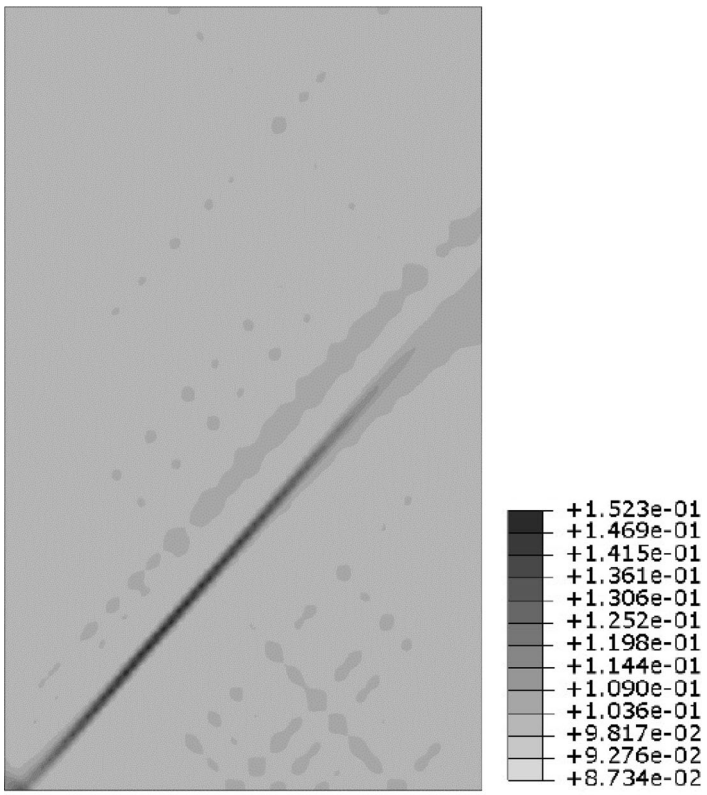
+1.523e-01
+1.469e-01
+1.415e-01
+1.361e-01
+1.306e-01
+1.252e-01
+1.198e-01
+1.144e-01
+1.090e-01
+1.036e-01
+9.817e-02
+9.276e-02
+8.734e-02

(a)

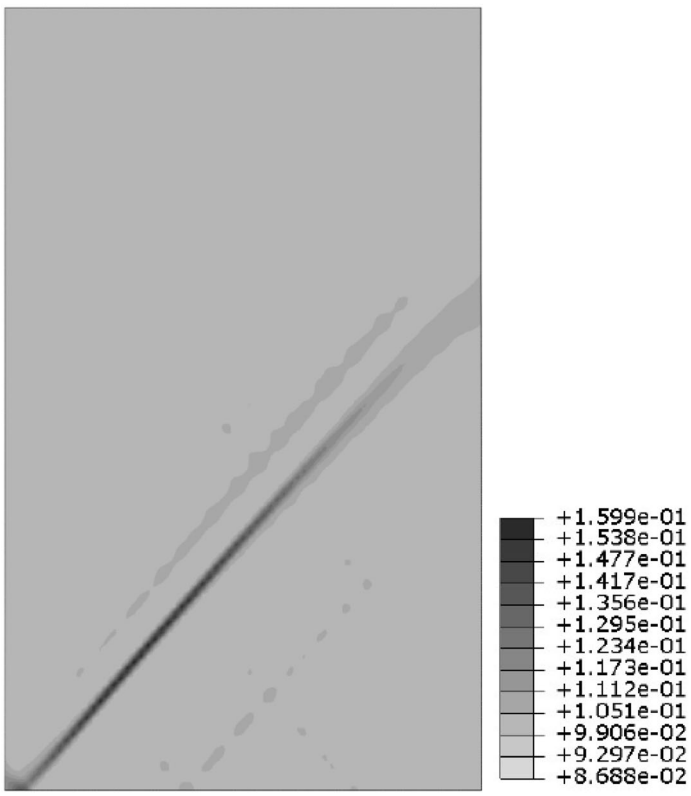
+1.599e-01
+1.538e-01
+1.477e-01
+1.417e-01
+1.356e-01
+1.295e-01
+1.234e-01
+1.173e-01
+1.112e-01
+1.051e-01
+9.906e-02
+9.297e-02
+8.688e-02

(b)

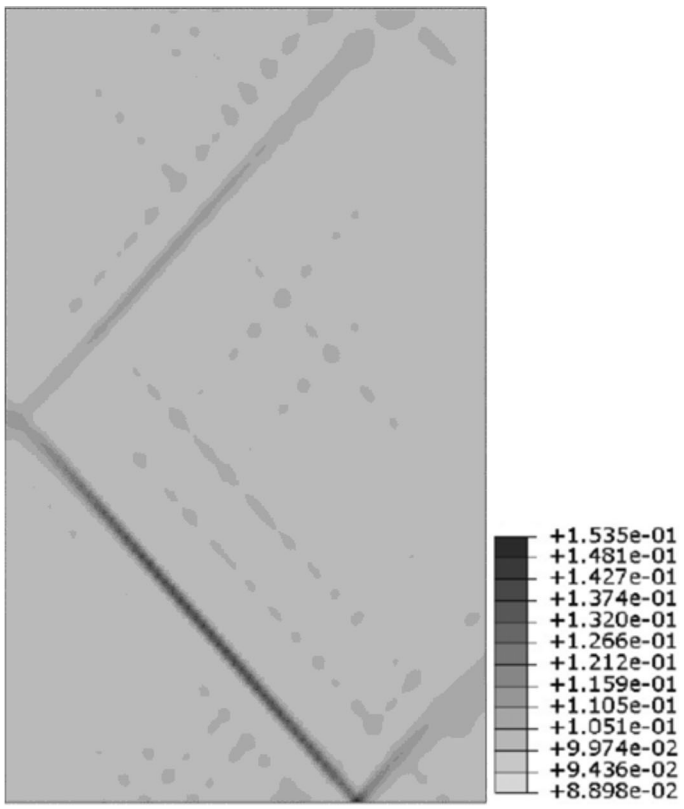
+1.535e-01
+1.481e-01
+1.427e-01
+1.374e-01
+1.320e-01
+1.266e-01
+1.212e-01
+1.159e-01
+1.105e-01
+1.051e-01
+9.974e-02
+9.436e-02
+8.898e-02

(a)

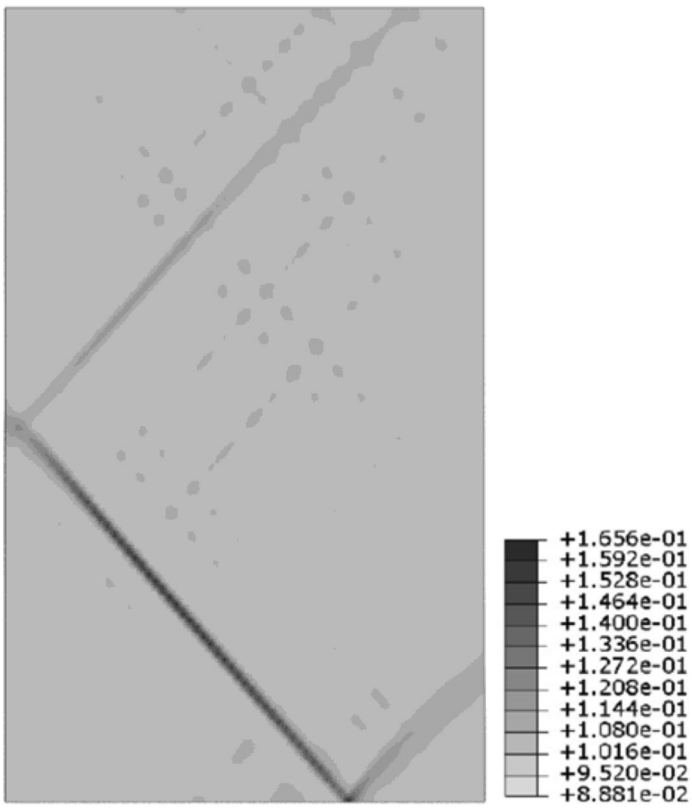
+1.656e-01
+1.592e-01
+1.528e-01
+1.464e-01
+1.400e-01
+1.336e-01
+1.272e-01
+1.208e-01
+1.144e-01
+1.080e-01
+1.016e-01
+9.520e-02
+8.881e-02

(b)

◀**Fig. 13** Shear band developed for two different mesh discretizations with the number of elements **a** 7938 and **b** 9800 which are simulated at 0.1/s strain rate, $e_0 = 0.9$ and $\sigma_c = 100$ kPa with heterogeneity induced at mid-point of the leftmost surface (shear strain contour at 8.8% global axial strain)

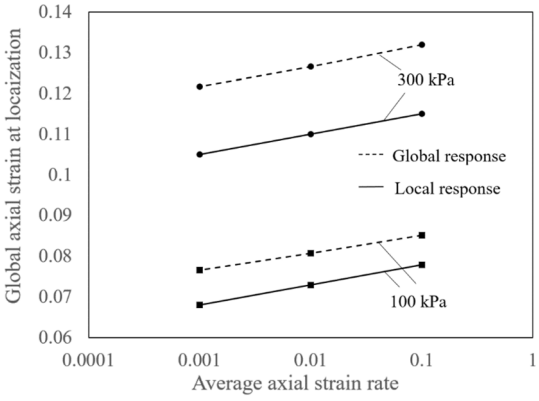

(a)

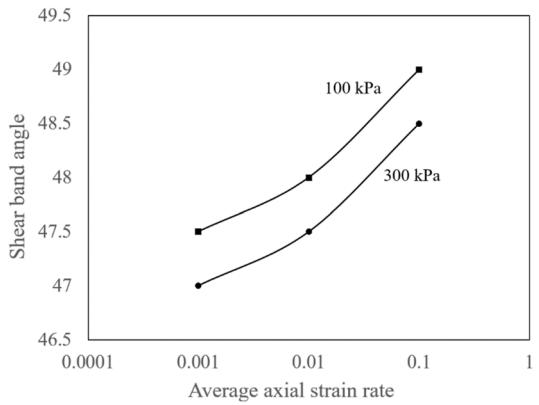

(b)

Fig. 14 Variation in **a** global axial strain at localization (considering both global and local response) and **b** shear band angle with strain rate at two initial confining pressures for $e_0 = 0.9$

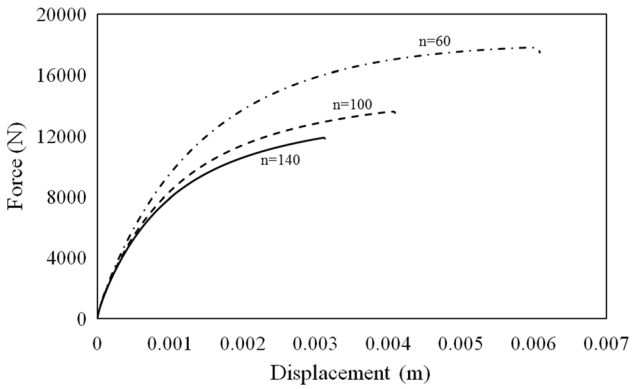

Fig. 15 Force–displacement curves obtained from 2D plane-strain simulations at different n values for a case with $e_0 = 0.9$ and 100 kPa initial confining pressure

100 kPa confining pressure, band angle increases from 47.5° to 49° (measured anticlockwise from horizontal) as strain rate increases from 0.001 to 0.1/s, whereas bifurcation-based rate-independent instability analysis predicts a shear band angle of 47.6° [33]. Unlike band angle, the shear band thickness remains independent of the strain rate. The deformed profile indicates that the shear band orientation and location do not vary much during the shearing process but subsequent variation is observed in the magnitude of shear strain developed within the localized zone. The present study aims to explore influence of strain rate on the emergence of localization and initial shear band angle. Post-bifurcation analysis has not been carried out here, and hence, subsequent growth and change in inclination of shear band angle with continued shearing have not been examined. Convergence issues are noticed in the post-peak regime while performing simulations at lower strain rate or with parameter values indicating low rate sensitivity.

The effect of rate sensitivity of the material on localization has been studied by varying the n parameter. Simulations has been performed for three values of strain rate exponent,$n = 60$, 100 and 140 at 0.1/s rate, and the force–displacement curves are presented in Fig. 15 for 100 kPa initial confining pressure. Similar to higher rates, a lower value of n, i.e., higher rate-sensitivity, retards the localization onset and results in an increase in the shear band angle (Fig. 16). This nature remains unchanged even for other confining pressures.

Figure 17 presents the force–displacement relationship at two different strain rates, 0.0001 and 0.00001/s, for a denser state with $e_0 = 0.65$ and 100 kPa initial confining pressure ($n = 60$ and $\dot{\varepsilon}_{\text{ref}} = 1 \times 10^{-6}$/s). Similar to loose state, the localization is observed to get retarded with an increase in the strain rate; however, in this case localization forms in the post-peak regime. It is important to note that this behavior is markedly different than the localization emergence in rate-independent case, where localized instabilities are captured in the hardening regime. The shear band angle in the dense sand is also noticed to increase slightly, i.e., from 46° to 46.5° (measured anticlockwise from horizontal) as the strain rate increases from 0.00001 to 0.0001/s. The simulations in dense sand with higher strain rates ($\geq$ 0.001/s) do not lead to localization even when shearing is continued till 20% global axial strain. The assumption of small deformation no longer remains valid beyond such strain level, and hence, localized instabilities in dense sand for higher strain rates are not further explored.

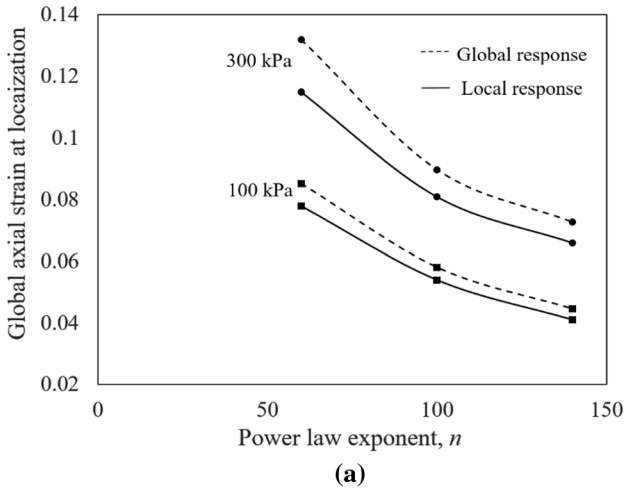

(a)

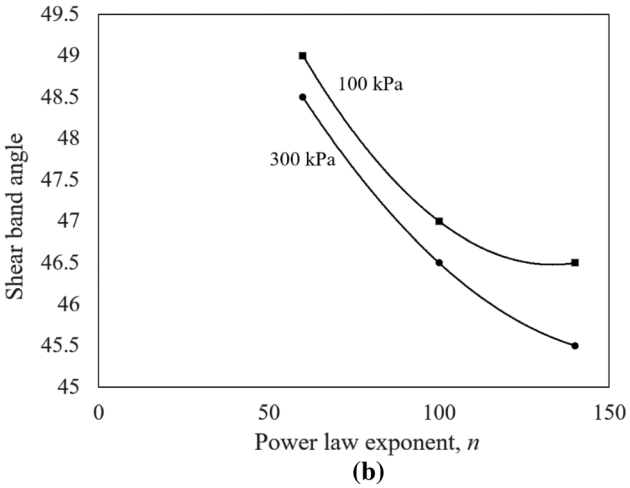

(b)

Fig. 16 Variation in **a** global axial strain at localization (considering both global and local response) and **b** shear band angle with power law exponent, n at two initial confining pressures for $e_0 = 0.9$

5 Conclusion

A material model has been proposed to predict the rate-sensitive stress–strain behavior of soil and implemented further in a finite element framework to explore the influence of strain rate on the localization behavior of sand. The proposed model simulates various constitutive features of sand subjected to higher strain rate as reported in the existing literature. This includes rate-induced strength increase along with early peaks and reduced compressive response in loose sand. At reference strain rate, the stress–strain response predicted from the rate-dependent analysis becomes comparable with the same from rate-independent one. It is important to note that the proposed model can be used for predicting rate-dependent response over both low and high range of strain rate, provided the rate parameters are selected carefully over the considered strain rate regime. In addition to it, the change in rate-sensitive response of sand over different density states can also be incorporated by calibrating the rate parameter, n over different material states.

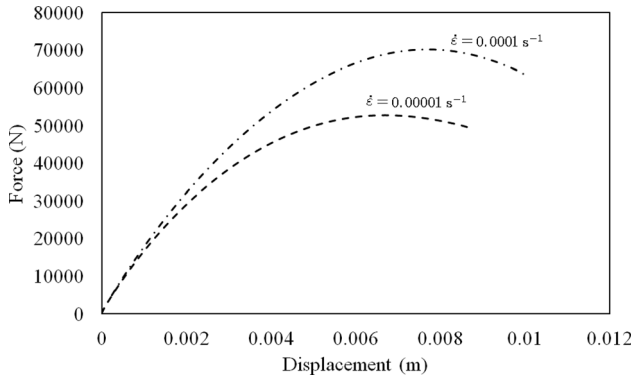

Fig. 17 Force–displacement curves obtained from 2D plane-strain simulations at two different strain rates for a case with $e_0 = 0.65$ and 100 kPa initial confining pressure

The drop in the force–displacement curve is generally considered to indicate the initiation of localization in finite element simulations; however, the local strain variations are noticed here to give an early prediction of bifurcation onset. An increase in the strain rate leads to a delayed onset of strain localization along with an increase in the shear - band angle. Strains are noticed to localize in the hardening regime for loose sand, whereas for denser state localization emerges in the post-peak regime. The thickness of the shear band is observed to be independent of the size of the mesh discretization.

Acknowledgements The authors would like to acknowledge the insightful discussions with Dr. Arghya Das from Indian Institute of Technology Kanpur regarding the numerical implementation of the proposed model in ABAQUS. The authors wish to thank SERB (Grant No. ECR/2018/002141) for the financial support toward carrying out part of this research.

Appendix

In case of plastic or viscoplastic material response, the nonlinear stress–strain relations are generally evaluated incrementally. Following the approach given in Wang et al. [52], this section presents a one-step Euler stress-update algorithm for the proposed Perzyna-type viscoplastic model. In case of small deformation formulation, the incremental strain $\Delta\varepsilon$ can be decomposed into an elastic part $\Delta\varepsilon^e$ and a viscoplastic part $\Delta\varepsilon^{vp}$ according to

$$\Delta\varepsilon = \Delta\varepsilon^e + \Delta\varepsilon^{vp}. \tag{8}$$

In case of proposed model, flow rule is defined by

$$\dot{\varepsilon}^{vp} = \dot{\varepsilon}_{\text{ref}}\phi\bar{n}, \text{ where } \bar{n} = \partial g_d \Big/ \partial\sigma' \text{ and } \phi = \left(\eta_{yd}/\eta_{ys}\right)^n. \tag{9}$$

The incremental stress is related to the elastic response by

$$\Delta\sigma' = E(\Delta\varepsilon - \Delta\varepsilon^{vp}) \ , \tag{10}$$

where E represents the elastic stiffness tensor. A generalized trapezoidal rule can be applied to estimate the incremental viscoplastic strain and change in the internal state variable

$$\begin{aligned} \Delta\varepsilon^{vp} &= \left[(1-\bar{\theta})\dot{\varepsilon}_t^{vp} + \bar{\theta}\dot{\varepsilon}_{t+\Delta t}^{vp}\right]\Delta t \ , \\ \Delta\bar{\kappa} &= \left[(1-\bar{\theta})\dot{\bar{\kappa}}_t + \bar{\theta}\dot{\bar{\kappa}}_{t+\Delta t}\right]\Delta t \ , \end{aligned} \tag{11}$$

where $\bar{\kappa}$ denotes the internal variable of the viscoplastic model, and for the proposed model, two internal variables are considered, i.e., $\Delta\bar{\kappa}_1 = \varepsilon_q^{vp}$ and $\Delta\bar{\kappa}_2 = \varepsilon_p^{vp}$. The interpolation parameter, $\bar{\theta}$, is such that $0 \le \bar{\theta} \le 1$, where $\bar{\theta} = 0$ implies a complete explicit method and $\bar{\theta} = 1$ stands for the fully implicit method. In the one-step Euler integration scheme, the viscoplastic strain rate at the end of the time interval Δt is expressed in a limited Taylor series expansion as

$$\begin{aligned} \dot{\varepsilon}_{t+\Delta t}^{vp} &= \dot{\varepsilon}_t^{vp} + \left[\frac{\partial\dot{\varepsilon}^{vp}}{\partial\sigma'}\right]_t \Delta\sigma' + \left[\frac{\partial\dot{\varepsilon}^{vp}}{\partial\bar{\kappa}}\right]_t \Delta\bar{\kappa} \\ &= \dot{\varepsilon}_t^{vp} + \hat{G}_t\Delta\sigma' + h_t\Delta\bar{\kappa} \ , \end{aligned} \tag{12}$$

$$\text{where } \hat{G}_t = \dot{\varepsilon}_{\text{ref}}\left[\frac{\partial\phi}{\partial\sigma'}\bar{n}^T + \phi\frac{\partial\bar{n}}{\partial\sigma'}\right]_t, \quad h_t = \dot{\varepsilon}_{\text{ref}}\left[\frac{\partial\phi}{\partial\bar{\kappa}}\bar{n}\right]_t. \tag{13}$$

Substitution of Eq. 12 into Eq. 11 yields

$$\Delta\varepsilon^{vp} = \left(\dot{\varepsilon}_t^{vp} + \bar{\theta}\hat{G}_t\Delta\sigma' + \bar{\theta}h_t\Delta\bar{\kappa}\right)\Delta t \, . \tag{14}$$

Further substitution of Eq. 14 into the incremental stress–strain relation of Eq. 10 leads to the following relation:

$$\Delta\sigma' = D_c\Delta\varepsilon - \Delta\bar{q} \ , \tag{15}$$

$$\begin{aligned} \text{where } D_c &= \left[E^{-1} + \bar{\theta}\Delta t\hat{G}_t\right]^{-1} \ , \\ \Delta\bar{q} &= E\left(\dot{\varepsilon}_t^{vp}\Delta t + \bar{\theta}\Delta t h_t\Delta\bar{\kappa}\right) \ . \end{aligned} \tag{16}$$

The tensor D_c is the algorithmic tangent stiffness tensor. Following are the expressions derived for updating the stress–strain relation of the proposed model

$$\begin{aligned} \frac{\partial g_d}{\partial\sigma'_{ij}} &= \sqrt{\frac{3}{2}}\frac{S_{ij}}{\sqrt{S_{kl}S_{kl}}} + \frac{\delta_{ij}}{3}\left(M_c - \eta_{\text{yd}}\right), \\ &\text{where } S_{ij} = \sigma'_{ij} - \frac{\sigma'_{kk}\delta_{ij}}{3}, \eta_{\text{yd}} = \frac{3\sqrt{3J_2}}{I_1'} \ , \\ \frac{\partial^2 g_d}{\partial\sigma'_{ij}\partial\sigma'_{pq}} &= \sqrt{\frac{3}{2}}\left[-\frac{S_{ij}S_{pq}}{2\left(S_{kl}S_{kl}\right)^{3/2}} + \frac{\delta_{pi}\delta_{qj} - \delta_{ij}\delta_{pq}/3}{\sqrt{S_{kl}S_{kl}}}\right] \\ &\quad - \frac{\delta_{ij}}{3}\frac{\partial\eta_{\text{yd}}}{\partial\sigma'_{pq}} \ , \\ \frac{\partial\eta_{\text{yd}}}{\partial\sigma'_{pq}} &= \sqrt{\frac{3}{2}}\frac{3S_{pq}}{I_1'\sqrt{S_{kl}S_{kl}}} - \frac{3\sqrt{3J_2}\delta_{pq}}{\left(I_1'\right)^2} \ , \\ \hat{G}_{ijpq} &= n\dot{\varepsilon}_{\text{ref}}\frac{\left(\eta_{\text{yd}}\right)^{n-1}}{\left(\eta_{\text{ys}}\right)^n}\frac{\partial\eta_{\text{yd}}}{\partial\sigma'_{pq}}\frac{\partial g_d}{\partial\sigma'_{ij}} + \dot{\varepsilon}_{\text{ref}}\left(\frac{\eta_{\text{yd}}}{\eta_{\text{ys}}}\right)^n\frac{\partial^2 g_d}{\partial\sigma'_{ij}\partial\sigma'_{pq}} \ , \\ h_{ij}\Delta\bar{\kappa} &= -n\dot{\varepsilon}_{\text{ref}}\frac{\left(\eta_{\text{yd}}\right)^n}{\left(\eta_{\text{ys}}\right)^{n+1}}\left[\frac{\partial\eta_{\text{ys}}}{\partial\bar{\kappa}_1}\Delta\bar{\kappa}_1 + \frac{\partial\eta_{\text{ys}}}{\partial\bar{\kappa}_2}\Delta\bar{\kappa}_2\right]\frac{\partial g_d}{\partial\sigma'_{ij}} \ , \\ \text{and } \frac{\partial\eta_{\text{ys}}}{\partial\bar{\kappa}_1} &= \frac{\left(\eta_{\text{ps}} - \eta_{\text{ys}}\right)^2}{a\eta_{\text{ps}}} \ , \ \frac{\partial\eta_{\text{ys}}}{\partial\bar{\kappa}_2} = \frac{\eta_{\text{ys}}}{\eta_{\text{ps}}}\kappa v_0 \ . \end{aligned} \tag{17}$$

The stress increase for a given strain increment can be calculated from Eq. 16 along with Eq. 17, and subsequently, the viscoplastic strain increment can be estimated from Eq. 12. A complete explicit stress-point integration scheme has been adopted in the present work with $\bar{\theta} = 0$. It is important to note that such an explicit integration scheme, also known as forward Euler scheme, is conditionally stable and requires smaller discretization step while performing the time integration. Alternatively, an implicit-type time integration scheme, which is usually more robust and unconditionally stable, can also be employed for this purpose [10].

References

1. Abrantes AE, Yamamuro JA (2002) Experimental and data analysis techniques used for high strain rate tests on cohesion less soil. Geotech Test J 25(2):128–141
2. Andrade JE, Borja RI (2006) Capturing strain localization in dense sands with random density. Int J Numer Methods Eng 67:1531–1564
3. Andrade JE, Borja RI (2006) Modeling deformation banding in dense and loose fluid-saturated sands. Finite Elem Anal Des 43:361–383
4. Andrade JE, Chen Q, Le PH, Avila CF, Evans TM (2012) On the rheology of dilative granular media: bridging solid- and fluid-like behaviour. J Mech Phys Solids 60:1122–1136
5. Bang DPV, Di Benedetto H, Duttine A, Ezaoui A (2007) Viscous behaviour of dry sand. Int J Numer Anal Methods Geomech 31:1631–1658
6. Bigoni D (2012) Nonlinear solid mechanics bifurcation theory and material instability. Cambridge University Press, Cambridge

7. Borja RI, Andrade JE (2006) Critical state plasticity. Part VI: Meso-scale finite element simulation of strain localization in discrete granular materials. Comput Methods Appl Mech Eng 195:5115–5140
8. Borja RI, Song X, Rechenmacher AL, Abedi S, Wu W (2013) Shear band in sand with spatially varying density. J Mech Phys Solids 61(1):219–234
9. Borja RI, Song X, Wu W (2013) Critical state plasticity. Part VII: Triggering a shear band in variably saturated porous media. Comput Methods Appl Mech Eng 261–262:66–82
10. Borja RI, Yin Q, Zhao Y (2020) Cam-clay plasticity. Part IX: On the anisotropy, heterogeneity, and viscoplasticity of shale. Comput Methods Appl Mech Eng 360:112695
11. Boukpeti N, Mroz Z, Drescher A (2004) Modeling rate effects in undrained loading of sands. Can Geotech J 41(2):342–350
12. Carosio A, Willam K, Etse G (2000) On the consistency of viscoplastic formulations. Int J Solids Struct 37:7349–7369
13. Casagrande A, Shannon WL (1949) Strength of soils under dynamic loads. Trans ASCE 114:755–772
14. de Souza Neto EA, Peric D, Owen DRJ (2008) Computational methods for plasticity: theory and applications. Wiley, New York
15. Desai CS, Zhang D (1987) Viscoplastic models for geologic materials with generalized flow rule. Int J Numer Anal Methods Geomech 11:603–620
16. Di Benedetto H, Tatsuoka F, Ishihara M (2002) Time dependent shear deformation characteristics of sand and their constitutive modelling. Soils Found 42(2):1–22
17. Di Prisco C, Imposimato S (1996) Time dependent mechanical behavior of loose sands. Mech Cohes Frict Mater 1:45–73
18. Etse G, Willam K (1999) Failure analysis of elastoviscoplastic material models. J Eng Mech 125(1):60–69
19. Gajo A, Wood DM (1999) A kinematic hardening constitutive model for sands: the multiaxial formulation. Int J Numer Anal Methods Geomech 23:925–965
20. Garagash DI (2005) Diffused vs. localized instability in compacting geomaterials under undrained conditions. In: Geomechanics, testing, modelling and simulation, proceedings of the first Japan-U.S. Workshop on testing, modelling and simulation, Boston, Massachusetts, June 27–29, 2003. ASCE Geotechnical Special Publication No. 143, pp 444–462
21. Han C, Vardoulakis IG (1991) Plane-strain compression experiments on water-saturated fine-grained sand. Geotechnique 41(1):49–78
22. Heeres OM, Suiker ASJ, de Borst R (2002) A comparison between the Perzyna viscoplastic model and the consistency viscoplastic model. Eur J Mech A Solids 21:1–12
23. Higgins W, Chakraborty T, Basu D (2013) A high strain-rate constitutive model for sand and its application in finite-element analysis of tunnels subjected to blast. Int J Numer Anal Methods Geomech 37:2590–2610
24. Hinchberger SD, Qu G (2009) Viscoplastic constitutive approach for rate-sensitive structured clays. Can Geotech J 45(6):609–629
25. Jackson JG, Ehrgott JQ, Rohani B (1980) Loading rate effects on compressibility of sand. J Geotech Eng Div 106(GT8):839–852
26. Karimpour H, Lade PV (2010) Time effects relate to crushing in sand. J Geotech Geoenviron Eng ASCE 136(9):1209–1219
27. Katona M (1984) Evaluation of viscoplastic cap model. J Geotech Eng 110(8):1106–1125
28. Kiyota T, Tatsuoka F (2006) Viscous property of loose sand in triaxial compression, extension and cyclic loading. Soils Found 46(5):665–684
29. Kongkitkul W, Tatsuoka F, Duttine A, Kawabe S, Enomoto T, Di Benedetto H (2008) Modelling and simulation of rate-dependent stress-strain behavior of granular materials in shear. Soils Found 48(2):175–194
30. Lade PV, Liggio CD, Jungman N (2009) Strain rate, creep, and stress drop-creep experiments on crushed coral sand. J Geotech Geoenviron Eng 135(7):941–953
31. Lade PV, Karimpour H (2010) Static fatigue controls particle crushing and time effects in granular materials. Soils Found 50(5):573–583
32. Lee KL, Seed HB, Dunlop P (1969) Effect of transient loading on the strength of sand. In: Proceedings of the 7th international conference on soil mechanics and foundation engineering, Mexico, 1969. vol 1, pp 239–247
33. Mukherjee M, Gupta A, Prashant A (2016) Drained instability analysis of sand under biaxial loading using a 3D material model. Comput Geotech 79:130–145
34. Mukherjee M, Gupta A, Prashant A (2017) Instability analysis of sand under undrained biaxial loading with rigid and flexible boundary. Int J Geomech. https://doi.org/10.1061/(asce)gm.1943-5622.0000690
35. Needleman A (1988) Material rate dependence and mesh sensitivity in localization problems. Comput Methods Appl Mech Eng 67:69–85
36. Neilsen MK, Schreyer HL (1993) Bifurcations in elastic-plastic materials. Int J Solids Struct 30:521–544
37. Oka F, Kimoto S, Higo Y, Ohta H, Sanagawa T, Kodaka T (2011) An elasto-viscoplastic model for diatomaceous mudstone and numerical simulation of compaction bands. Int J Numer Anal Methods Geomech 35(2):244–263
38. Omidvar M, Iskander M, Bless S (2012) Stress–strain behavior of sand at high strain rates. Int J Impact Eng 49:192–213
39. Peng F-L, Siddiquee MSA, Tatsuoka F, Yasin SJM, Tanaka T (2009) Strain energy-based elasto-viscoplastic constitutive modelling of sand for numerical simulation. Soils Found 49(4):611–630
40. Perzyna P (1963) The constitutive equations for rate sensitive plastic materials. Quart Appl Math 20:321–332
41. Perzyna P (1966) Problems in viscoplasticity. Adv Appl Mech 9:244–368
42. Pierce D, Shih CF, Needleman A (1984) Tangent modulus method for rate dependent solids. Comput Struct 18(5):875–887
43. Prashant A, Penumadu D (2005) Effect of overconsolidation and anisotropy of Kaolin Clay using true triaxial testing. Soils Found 45(3):71–82
44. Regueiro RA, Foster CD (2011) Bifurcation analysis for a rate-sensitive, non-associative, three-invariant, isotropic/kinematic hardening cap plasticity model for geomaterials: part I. Small strain. Int J Numer Anal Methods Geomech 35:201–225
45. Rudnicki JW, Rice JR (1975) Conditions for the localization of deformation in pressure-sensitive dilatants materials. J Mech Phys Solids 23:371–394
46. Suescun-Florez E, Iskander M (2017) Effect of fast constant loading rates on the global behavior of sand in triaxial compression. Geotech Test J 40(1):52–71
47. Suescun-Florez E, Omidvar M, Iskander M, Bless S (2015) Review of high strain rate testing of granular soils. Geotech Test J 38(4):1–26
48. Simo JC, Hughes TJR (2000) Computational inelasticity. Springer, New York
49. Szabó L (2000) Comments on loss of strong ellipticity in elastoplasticity. Int J Solids Struct 37:3775–3806
50. Tatsuoka F, Ishihara M, Di Benedetto H, Kuwano R (2002) Time dependent shear deformation characteristics of geomaterials and their simulation. Soils Found 42(2):103–129
51. Tong X, Tuan C (2007) Viscoplastic cap model for soils under high strain rate loading. J Geotech Geoenviron Eng 133(2):206–214

52. Wang WM, Sluys LJ, De Borst R (1997) Viscoplasticity for instabilities due to strain softening and strain-rate softening. Int J Numer Methods Eng 40:3839–3864
53. Watanabe K, Kusakabe O (2013) Reappraisal of loading rate effects on sand behavior in view of seismic design for pile foundation. Soils Found 53(2):215–231
54. Whitman RV, Healy K (1962) The shearing resistance of sands during rapid loading. Trans ASCE 128(1):1553–1594
55. Whitman RV (1957) The behavior of soils under transient loading. In: Proceedings of the 4th international conference on soil mechanics, London, 1957. vol 1, pp 207–210
56. Wood DM (2004) Geotechnical modelling. Taylor and Francis group, CRC Press, Boca Raton
57. Wood DM, Belkheir K, Liu DF (1994) Strain softening and state parameter for sand modelling. Geotechnique 44(2):335–339
58. Yamamuro JA, Lade PV (1993) Effects of strain rate on instability of granular soils. Geotech Test J ASTM 16(3):304–313
59. Yamamuro JA, Abrantes AE, Lade PV (2011) Effect of strain rate on the stress-strain behavior of sand. J Geotech Geoenviron Eng ASCE 137(12):1169–1178